

# Predictions of gas/particle flow with an Eulerian model including a realistic particle size distribution

Vidar Mathiesen<sup>a,b</sup>, Tron Solberg<sup>a,c</sup>, Bjørn H. Hjertager<sup>a,c,\*</sup>

<sup>a</sup> *Telemark Technological R&D Centre (Tel-Tek), N-3914 Porsgrunn, Norway*

<sup>b</sup> *Telemark University College (HiT-TF), N-3914 Porsgrunn, Norway*

<sup>c</sup> *Aalborg University Esbjerg, DK-6700 Esbjerg, Denmark*

---

## Abstract

This paper presents a computational study of the flow behavior in a cold-flow pilot-scale circulating fluidized bed. A multi-fluid Computational Fluid Dynamics (CFD) model has been developed and verified against experimental data reported in the literature. The flow model is based on an Eulerian description of the phases where the kinetic theory of granular flow forms the basis for the turbulence modelling in the solid phases. The model is generalized for one gas phase and  $N$  number of solid phases to enable a realistic description of the particle size distributions in gas/solids flow systems. Each solid phase is characterized by a diameter, density and restitution coefficient. The simulations are performed with different superficial gas velocities, initial solids concentrations and standard deviations of the particle size distribution. Most emphasis is given to study the effects of different particle size distributions and to study the fluctuating behavior of the dilute gas/solids flow system. Altogether, the simulation results are in very good agreement with experimental data. Both mean diameters, axial and radial mean and turbulent velocities, and mass fluxes are calculated successfully. © 2000 Elsevier Science S.A. All rights reserved.

**Keywords:** Eulerian CFD model; Kinetic theory of granular flow; Gas–particle flow; Circulating fluidized bed

---

## 1. Introduction

Many industrial fluid flow processes include multiphase gas/particle phenomena. Numerical simulation of these multiphase flow processes provides a new tool for design and optimization of e.g. chemical reactors, such as fluidized bed systems. Computational Fluid Dynamics (CFD) techniques are derived from the equations governing the fluid flow, in the form of partial differential equations representing the conservation of mass, momentum and energy. The partial differential equations are reduced to an approximate and equivalent set of algebraic equations, which are solved numerically to give the flow field at discrete points in the calculation domain. Although CFD models are fairly well established for single phase flow,

multiphase flow and complex geometries make the solution even more challenging. However, CFD in multiphase flow has during the recent years become more accepted in modelling of gas/solids flow systems, and much progress has been made toward developing computer codes which calculate the flow behavior of fluidized beds. Most models reported in the literature are based on a two-phase description, one gas and one solid phase, where all the particles are assumed to have identical diameter, density and restitution coefficient. Normally a Eulerian description of the phases is given, where the constitutive equations describing the solid phases are based on kinetic theory for granular flow, e.g. Ref. [1]. Ref. [2] did simulations of a circulating fluidized bed using both Lagrangian and Eulerian approaches to describe the granular material. They demonstrated that, at the present time, the Eulerian approach is preferable when considering gas/solids flow systems such as fluidized beds. Ref. [3] have given a general review of different Eulerian two-phase flow models applied to fluidization.

In gas/solids flow systems, particle segregation due to different size and/or density will affect the flow behavior

---

\* Corresponding author. Chemical Engineering Laboratory, Aalborg University Esbjerg (AAUE), Niels Bohrs Vej 8, 6700 Esbjerg, Denmark. Tel.: +45-79-12-7615; fax: +45-79-12-7677.

E-mail address: bhh@auc.auc.dk (B.H. Hjertager).

significantly. To describe such phenomena, an extension to multiple particle phases is essential. Ref. [4] extended the kinetic theory for granular flow to binary mixtures. Equipartition of energy was assumed with small correction for the individual phase temperatures. Based on this turbulence model, Ref. [5] developed a multiphase gas/solids flow model and performed simulations with one gas and three solid phases. The model predicted segregation effects fairly well and a good agreement with experimental data was demonstrated.

Refs. [6] and [7] extended the kinetic theory to binary mixtures of solids with unequal granular temperatures between the phases, where each solid phase is uniquely defined by particle diameter, density and restitution coefficient. Based on their research, Ref. [8] proposed a modified multiphase gas/particle flow model. The model was generalized and made consistent for one gas phase and  $N$  number of solid phases to enable description of realistic particle size distribution.

In this work, the flow model is presented and applied to simulation of a cold-flow pilot-scale circulating fluidized bed. Three solid phases (with different particle diameters) are used to enable a realistic description of the particle size distribution. The numerical results are discussed and compared against the experimental data of Ref. [9].

## 2. Experimental setup

A detailed description of the circulating fluidized bed system and measurement techniques is given by Ref. [9]. Fig. 1 gives a sketch of the experimental setup.

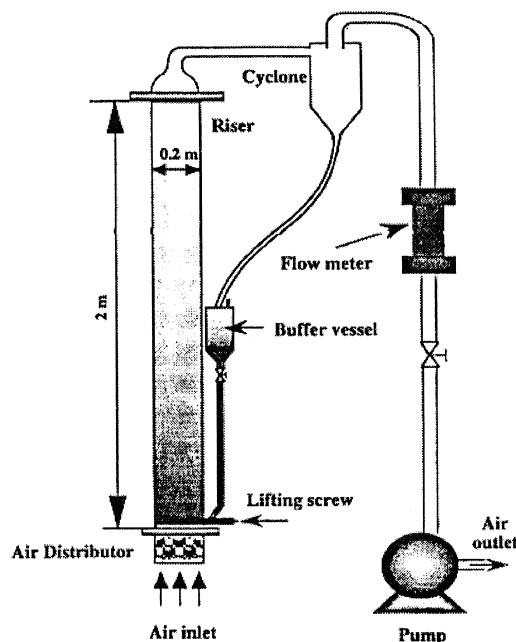


Fig. 1. The experimental setup [9].

The riser has a cross-sectional area of  $0.2 \times 0.2 \text{ m}^2$  and is 2.0 m high. The primary air inlet is located at the bottom of the riser where the gas is passing through an air distributor to provide a uniform flow of air. The air has ambient temperature and pressure. At the top of the riser the suspended glass particles enter a cyclone and are recycled via a return loop.

Ref. [9] used laser Doppler anemometry (LDA) and phase Doppler anemometry (PDA) measurement techniques to measure flow parameters, such as mean diameter, particle flux and mean and fluctuating velocities. LDA/PDA is a non-invasive optical technique that does not disturb the flow, has a high spatial resolution with a fast dynamic response and range. The particle velocity measurement is based upon that when two coherent Gaussian laser beams are intersecting each other; the intersection will cause interference fringes. The particle velocity of a passing particle will be the Doppler frequency times the fringe spacing. The Doppler frequency is obtained by a photo detector. The particle size may be measured using the PDA system. The technique is based upon that when two adjacent photo detectors are used to collect scattered laser light; they will show a phase difference that is linearly proportional to the diameter of a smooth and spherical particle as passing through the measuring volume.

The experiments were performed with two different particle size distributions with a constant mean particle diameter at  $120 \text{ }\mu\text{m}$ . The measurements were conducted with two different superficial gas velocities, 0.7 and 1.0 m/s, respectively. The initial solids concentration in the gas/solids system was dilute with a solids concentration of 1% and 3% of the riser volume. Notice that all the experimental data was originally reported by Ref. [9].

## 3. CFD model

Based on an Eulerian description of the phases, a multiphase CFD model for turbulent gas/solids flow is presented. The Eulerian approach considers the gas as well as each solid phase as continuum. In our model we used  $M$  phases, one gas and  $N$  solid phases. Each solid phase is uniquely defined by a diameter, density and restitution coefficient. The presence of each phase is described by a volume fraction, varying from zero to one.

The laws of conservation of mass, momentum and granular temperature are satisfied for each phase individually. The dependent variables, i.e. the volume fraction and the momentum, are solved for each phase. All the phases share a fluid pressure. The gas phase turbulence is modelled by a subgrid scale (SGS) model. The largest scales are simulated directly, and the small scales are modelled with the SGS turbulence model. A conservation equation for granular temperature (defined as one-third times the fluctuating velocity squared) is solved for each solid phase.

The transport equations for the continuous gas phase was derived from a control volume approach. For the solid phases, the Reynolds transport theorem was used to develop the well-known Boltzmann equation. A complete derivation of the equation for two-phase gas/particle flow is given by Ref. [1]. The particles are assumed inelastic, smooth, spherically and non-rotating. Moreover, based on the distribution of the particles, the constitutive relations, which close the transport equations are provided by this method. These constitutive laws specify how the physical parameters of the phases interact with each other. Ref. [7] gives an extension to binary mixtures of particulate materials and derives transport equations for each solid phase. His approach involved kinetic theory for binary granular mixtures with unequal granular temperatures between the phases. The constitutive equations come from the interactions of the fluctuating and the mean motion of the particles. The shear stresses are the sum of a collisional and a kinetic part. The pressure of the solid phases, which includes both kinetic and collisional pressures, were determined from an equation of state. In these expressions the restitution coefficient were introduced along with the radial distribution function. The shear viscosities for dilute and dense flow are a product of mean free path times an oscillation velocity times particle density. The coupling between the various particle phases is through particle pressures, binary radial distribution functions, viscosities, particle collision dissipations and conductivities. In addition to gas–particle drag, particle–particle drag is introduced in the model.

The mathematical model is incorporated in the CFD model, FLOTRACS-MP-3D, which is three-dimensional (3D) in Cartesian coordinates with the following governing conservation equations. A detailed description, including a discussion of the consistency of the multiphase gas/particle model is given by Ref. [8].

### 3.1. Governing equations

The mathematical model developed by Ref. [8] is summarized in this section.

#### 3.1.1. Continuity equations

The continuity equation for phase  $m$  is given by:

$$\frac{\partial}{\partial t}(\beta_v \varepsilon_m \rho_m) + \frac{\partial}{\partial x_i}(\beta_i \varepsilon_m \rho_m U_{i,m}) = 0 \quad (1)$$

where  $\varepsilon_m$ ,  $\rho_m$  and  $U_{i,m}$  are the phase volume fractions, densities and the  $i$ th direction velocity components, respectively.  $\beta_v$  is the volume porosity and  $\beta_i$  is the area porosity in  $i$ -th direction. The volume and area porosities have values between zero and unity, where zero is a totally blocked and unity is totally open. No mass transfer is allowed between the phases.

#### 3.1.2. Momentum equations

The momentum equations in the  $j$ -direction for phase  $m$  may be expressed as:

$$\begin{aligned} \frac{\partial}{\partial t}(\beta_v \varepsilon_m \rho_m U_{j,m}) + \frac{\partial}{\partial x_i}(\beta_i \varepsilon_m \rho_m U_{i,m} U_{j,m}) \\ = -(\beta_v \varepsilon_m) \frac{\partial P}{\partial x_j} + \frac{\partial}{\partial x_i}(\beta_i \Pi_{ij,m}) \\ + \beta_v \varepsilon_m \rho_m g_j + \beta_v \sum_{k=1, k \neq m}^M \Phi_{mk}(U_{j,k} - U_{j,m}) \end{aligned} \quad (2)$$

$P$  and  $g_j$  are fluid pressure and  $j$ -direction component of gravity, respectively.  $\Phi_{mk}$  is drag coefficient between the phases  $m$  and  $k$ . Hence, the terms on the right side represent pressure forces, viscous forces, mass forces and drag forces, respectively. Both gas–particle and particle–particle drag are included in the total drag.

We consider each phase as an incompressible fluid. But due to the extension to multiphase flow, the divergence term is included. Hence the stress tensor  $\Pi_{ij,g}$  for the gas phase  $g$  is given by:

$$\Pi_{ij,g} = \mu_{\text{eff},g} \left[ \left( \frac{\partial U_j}{\partial x_i} + \frac{\partial U_i}{\partial x_j} \right) - \frac{2}{3} \delta_{ij} \frac{\partial U_k}{\partial x_k} \right] \quad (3)$$

where  $\delta_{ij}$  is the Kroenecker delta. The gas phase turbulence is modelled by the SGS model proposed by Ref. [10]. The technique is a large eddy simulation (LES), where the largest scales are solved directly, whereas the small scales are modelled with the SGS turbulence model. Thus, the effective viscosity  $\mu_{\text{eff},g}$  may be estimated as:

$$\mu_{\text{eff},g} = \varepsilon_g \mu_{\text{lam},g} + \varepsilon_g \rho_g (c_t \Delta)^2 \sqrt{S_{ij,g} : S_{ij,g}} \quad (4)$$

$$\Delta = \sqrt[3]{\Delta x \Delta y \Delta z} \text{ and } S_{ij,g} = \frac{1}{2} \left[ \frac{\partial U_j}{\partial x_i} + \frac{\partial U_i}{\partial x_j} \right]_g$$

The turbulence model constant  $c_t$  is estimated to 0.079 by using the renormalization group (RNG) theory [11].  $\Delta$  is the characteristic length scale for the resolved eddies.

The total stress tensor  $\Pi_{ij,s}$  for each solid phase  $s$  is the sum of a collisional and a kinetic part:

$$\begin{aligned} \Pi_{ij,s} = -P_s \delta_{ij} + \mu_s \left( \frac{\partial U_j}{\partial x_i} + \frac{\partial U_i}{\partial x_j} \right)_s \\ + \left( \xi_s - \frac{2}{3} \mu_s \right) \delta_{ij} \left( \frac{\partial U_k}{\partial x_k} \right)_s \end{aligned} \quad (5)$$

Whereas the bulk viscosity is approximated to be zero for most gases, as done here the bulk viscosity  $\xi_s$  should be included when considering granular materials. The solid phase pressure  $P_s$ , which include a collisional and a kinetic term, is determined from an equation of state similar to

van der Waals equation of state for gases, and is the equation of state for a granular material:

$$P_s = \sum_{n=1}^N P_{C,sn} + \varepsilon_s \rho_s \theta_s \quad (6)$$

The pressure denoted  $P_{C,sn}$  is caused by collisions between the solid phases  $s$  and  $n$ , and has the expression:

$$P_{C,sn} = \frac{\pi}{3} (1 + e_{sn}) d_{sn}^3 g_{sn} n_s n_n \times \left\{ \frac{m_0 \theta_s \theta_n}{((m_s/m_n) \theta_s + (m_n/m_s) \theta_n)} \right\} \times \left\{ \frac{(m_0/m_s)^2 \theta_s \theta_n}{(\theta_s + (m_n/m_s)^2 \theta_n)(\theta_s + \theta_n)} \right\}^{3/2} \quad (7)$$

Here, the binary restitution coefficient, diameter and mass are defined respectively by:

$$e_{sn} = \frac{1}{2} (e_s + e_n) \quad (8)$$

$$d_{sn} = \frac{1}{2} (d_s + d_n)$$

$$m_0 = m_s + m_n$$

The restitution coefficient is unity for fully elastic and zero for plastic collisions. We assume the particles to be spherical. Hence the number of particles and the particle mass are given, respectively:

$$n_s = \frac{6\varepsilon_s}{\pi d_s^3} \text{ and } m_s = \frac{\pi d_s^3 \rho_s}{6} \quad (9)$$

The radial distribution function  $g_{sn}$  is an expression for the probability of particle collisions, and is near one when the flow is dilute and becomes infinite when the flow is so dense that motion is impossible. Based on the single solid phase model given implicitly by Ref. [12], Ref. [8] considers the binary radial distribution function as:

$$g_0 = \left\{ 1 - \left( \frac{1 - \varepsilon_g}{\varepsilon_{s,max}} \right)^{\frac{1}{3}} \right\}^{-1} \quad (10)$$

$$g_{sn} = \frac{N}{2} \frac{g_0}{(1 - \varepsilon_g)} (\varepsilon_s + \varepsilon_n)$$

where  $\varepsilon_{s,max}$  is the maximum total volume fraction of solids, in this work set to 0.63.

The solid phase bulk viscosity or volume viscosity may be written as:

$$\xi_s = \sum_{n=1}^N P_{C,sn} \frac{d_{sn}}{3} (\theta_s + (m_n/m_s) \theta_n) \times \sqrt{\frac{2}{\pi \theta_s \theta_n (\theta_s + (m_n/m_s)^2 \theta_n)}} \quad (11)$$

The solid phases shear viscosity,  $\mu_s$ , consists of a collisional term,  $\mu_{col,s}$  (which is proportional to the bulk viscosity):

$$\mu_{col,s} = \sum_{n=1}^N P_{C,sn} \frac{d_{sn}}{5} (\theta_s + (m_n/m_s) \theta_n) \times \sqrt{\frac{2}{\pi \theta_s \theta_n (\theta_s + (m_n/m_s)^2 \theta_n)}} \quad (12)$$

and a kinetic term:

$$\mu_{kin,s} = \frac{2\mu_{dil,s}}{\frac{1}{N} \sum_{n=1}^N (1 + e_{sn}) g_{sn}} \times \left\{ 1 + \frac{4}{5} \sum_{n=1}^N g_{sn} \varepsilon_n (1 + e_{sn}) \right\}^2 \quad (13)$$

where

$$\mu_{dil,s} = \frac{15}{8d_s^3} \varepsilon_s l_s \sqrt{\frac{2m_s \theta_{s,av}}{\pi}} \quad (14)$$

The mean free path  $l_s$  is given by:

$$l_s = \frac{1}{6\sqrt{2}} \frac{d_s}{\varepsilon_s} \quad (15)$$

To ensure that the dilute viscosity,  $\mu_{dil,s}$ , is finite as the volume fraction of solids approaches zero, the mean free path is limited by a characteristic dimension, in this work set to the minimum control volume length.

The average granular temperature denoted  $\theta_{s,av}$  is obtained from Ref. [7]:

$$\theta_{s,av} = \frac{2m_s \theta_s}{\left\{ \sum_{n=1}^N \left( \frac{n_n}{n_s} \right) \left( \frac{d_{sn}}{d_s} \right)^2 \sqrt{\frac{(m_0/m_s)^2 \theta_n}{(\theta_s + (m_n/m_s)^2 \theta_n)}} S^{3/2} \right\}^2} \quad (16)$$

$$S = \frac{(m_0/m_s)^2 \theta_s \theta_n}{(\theta_s + (m_n/m_s)^2 \theta_n)(\theta_s + \theta_n)}$$

For  $\varepsilon_g \leq 0.8$ , the gas–particle drag coefficient is based on the well-known Ergun equation [13]:

$$\Phi_{sg} = 150 \frac{\varepsilon_s (1 - \varepsilon_g) \mu_{\text{lam},g}}{\varepsilon_g d_s^2} + 1.75 \frac{\varepsilon_s \rho_g |\vec{u}_g - \vec{u}_s|}{d_s} \quad (17)$$

For  $\varepsilon_g > 0.8$ , the drag coefficient is based on the single sphere expression derived by [14]:

$$\Phi_{sg} = \frac{3}{4} C_d \frac{\varepsilon_s \varepsilon_g \rho_g |\vec{u}_g - \vec{u}_s|}{d_s} f(\varepsilon_g) \quad (18)$$

where

$$f(\varepsilon_g) = \varepsilon_g^{-2.65} \quad (19)$$

The relation given in Eq. (19) acts as a correction of the Stokes law for free fall of a single particle and is introduced due to the presence of other particles in the fluid [15]. The drag coefficient  $C_D$  is related to the Reynolds number by [16]:

$$C_d = \frac{24}{Re_s} (1 + 0.15 Re_s^{0.687}) \quad Re_s \leq 1000 \quad (20)$$

$$C_d = 0.44 \quad Re_s > 1000$$

$$Re_s = \frac{d_s \rho_g \varepsilon_g |\vec{u}_g - \vec{u}_s|}{\mu_{\text{lam},g}}$$

The particle–particle drag coefficient,  $\phi_{sn}$ , is proportional to the particle collisional pressure [7]:

$$\begin{aligned} \Phi_{sn} = P_{C,sn} & \left\{ \frac{3}{d_{sn}} \sqrt{\frac{2(m_s^2 \theta_s + m_n^2 \theta_n)}{\pi m_0^2 \theta_s \theta_n}} \right. \\ & + \frac{1}{|\vec{u}_n - \vec{u}_s|} \left[ \nabla \ln \frac{\varepsilon_s}{\varepsilon_n} + \frac{\theta_s \theta_n}{\theta_s + \theta_n} \left| \frac{\nabla \theta_n}{\theta_n^2} \right| \right. \\ & \left. \left. - \frac{\nabla \theta_s}{\theta_s^2} \right| + 3 \nabla \left| \frac{\ln(m_s \theta_n)}{\ln(m_s \theta_s)} \right| \right] \right\} \quad (21) \end{aligned}$$

### 3.1.3. Turbulent kinetic energy equations

Conservation equation for granular temperature is solved for each solid phase:

$$\begin{aligned} \frac{3}{2} \left[ \frac{\partial}{\partial t} (\beta_v \varepsilon_s \rho_s \theta_s) + \frac{\partial}{\partial x_i} (\beta_i \varepsilon_s \rho_s U_{i,s} \theta_s) \right] \\ = \beta_v \left( \Pi_{ij,s} \frac{\partial U_{j,s}}{\partial x_i} \right) + \frac{\partial}{\partial x_i} \left( \beta_i \kappa_s \frac{\partial \theta_s}{\partial x_i} \right) \\ - \beta_v \gamma_s - 3 \beta_v \Phi_{sg} \theta_s \quad (22) \end{aligned}$$

The terms on the right side of the equation represent production due to shear, diffusive transport of granular temperature, dissipation due to inelastic collisions and dissipation due to fluid friction. A corresponding produc-

tion term due to fluctuations in drag has been assumed negligible. This is a reasonable assumption for the relatively large and heavy glass particles considered in this work. Hence, the particle response time is assumed to be much longer than the characteristic time scale for the turbulent fluid motion.

The conductivity of granular temperature  $\kappa_s$ , and the dissipation due to inelastic collisions  $\gamma_s$  are determined from the kinetic theory for granular flow. The granular conductivity is given by a dilute and a dense part as:

$$\begin{aligned} \kappa_s = \frac{2 \kappa_{\text{dil},s}}{\frac{1}{N} \sum_{n=1}^N (1 + e_{sn}) g_{sn}} \left\{ 1 + \frac{6}{5} \sum_{n=1}^N g_{sn} \varepsilon_n (1 + e_n) \right\}^2 \\ + 2 \varepsilon_s \rho_s d_s \sqrt{\frac{\theta_s}{\pi}} \sum_{n=1}^N \varepsilon_n g_{sn} (1 + e_{sn}) \quad (23) \end{aligned}$$

where

$$\kappa_{\text{dil},s} = \frac{225}{32} \varepsilon_s l_s \sqrt{\frac{2 m_s \theta_{s,av}}{\pi}} \quad (24)$$

The first term in Eq. (23) dominates in dilute flow and the second term in dense regimes. As for the shear viscosity, the mean free path is limited by the minimum control volume length to ensure that the dilute granular conductivity is finite as the solid volume fraction approaches zero.

The dissipation of the turbulent kinetic energy due to particle collisions is given by:

$$\begin{aligned} \gamma_s = \sum_{n=1}^N \frac{3}{4} P_{C,sn} \frac{(1 - e_{sn})}{d_{sn}} \\ \times \left[ 4 \sqrt{\frac{2 \theta_s \theta_n}{\pi ((m_s/m_0)^2 \theta_s + (m_n/m_0)^2 \theta_n)}} \right. \\ \left. - d_{sn} \left( \frac{(m_s/m_0) \theta_s + (m_n/m_0) \theta_n}{((m_s/m_0)^2 \theta_s + (m_n/m_0)^2 \theta_n)} \right) \frac{\partial U_{k,s}}{\partial x_k} \right] \quad (25) \end{aligned}$$

The divergence term is often neglected, but we have retained it in our calculations. However, the term may cause production instead of dissipation, and is handled with special care.

### 3.2. Numerical solution procedure

The governing equations are solved by a finite volume method, where the calculation domain is divided into a finite number of non-overlapping control volumes. At main grid points placed in the center of the control volume, volume fraction, density, and turbulent kinetic energy are stored. A staggered grid arrangement is adopted for the velocity components that are stored at the main control volume surfaces. The conservation equations are integrated in space and time. This integration is performed using

upwind differencing in space and fully implicit in time. The set of algebraic equations is solved by the tridiagonal-matrix algorithm (TDMA), except for the volume fraction where a point iteration method is used. Due to the strong coupling between the phases through the drag forces, the two-phase partial elimination algorithm (PEA) [17], is generalized to multiple phases and used to decouple the drag forces. The IPSA (interphase-slip algorithm) is used to take care of the coupling between the continuity and the velocity equations [18].

### 3.3. Numerical flow parameters

The simulation geometry with internal obstructions and grid nodes is shown in Fig. 2. The 2D calculation domain is divided into  $38 \times 102$  grid nodes, in the radial and axial directions, respectively. The grid is chosen to be uniform in the axial direction, whereas a non-uniform grid is used in radial direction in order to have smaller control volumes where the gradients are expected to be large. Although a grid dependence study is clearly desirable, the long computational times involved make such a study not feasible. Based on previous experience, e.g. Refs. [19] and [20], the grid resolution appears nevertheless to be adequate.

To enable a realistic particle size distribution, three solid phases are used in the simulations. The Sauter mean particle diameter is held constant at  $120 \mu\text{m}$  and the standard deviations,  $\sigma$ , are 18 and  $40 \mu\text{m}$ , respectively. For the particle size distribution with a standard deviation of  $18 \mu\text{m}$ , the three solid phases I, II and III have diameters of 84, 120 and  $156 \mu\text{m}$ , respectively and a volume fractions of particles of 12.5%, 75.0% and 12.5%,

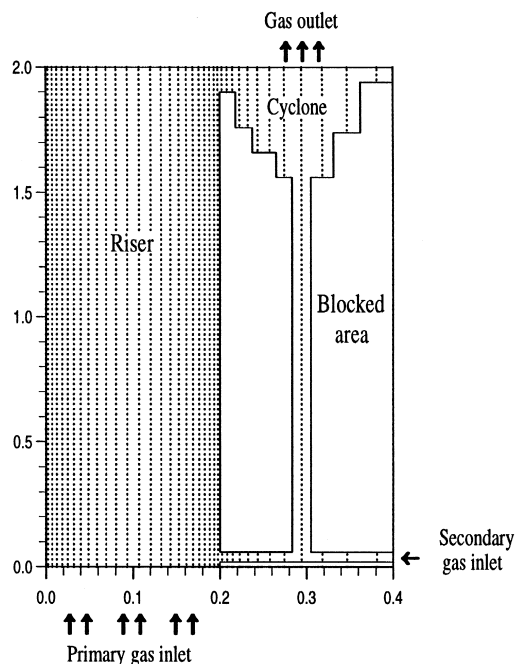


Fig. 2. Simulation geometry with internal obstructions and grid points.

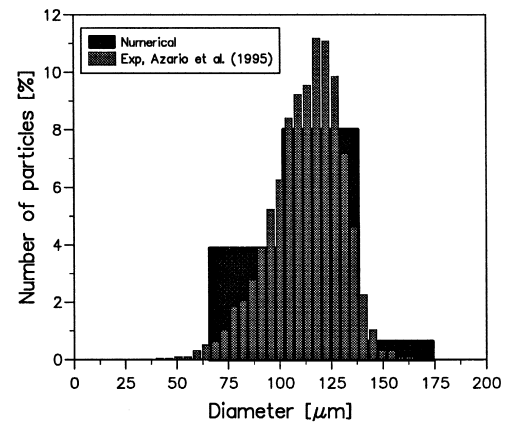


Fig. 3. Initial particle size distribution.

respectively. Fig. 3 shows the numerical and real particle size distribution with this standard deviation. A comparison shows that with three solid phases, the CFD-model is able to describe the real particle size distribution fairly well.

For the wide-ranging particle size distribution with a standard deviation of  $40 \mu\text{m}$ , the three solid phases I, II and III have diameters of 63, 120 and  $177 \mu\text{m}$ , respectively and a volume fraction of particles of 25.0%, 50.0% and 25.0%, respectively.

The particle density is  $2400 \text{ kg/m}^3$  and the restitution coefficient for all the solid phases are set to 1.0 in all simulations.

In order to get reasonable computational results to compare against the experimental data, time averaged results are obtained between 16 and 20 s of real simulation time.

The solid phases are initially perfectly mixed in the bed and the initial bed height depends on the concentration of solids.

The air inlets are modelled as 1D plug flow. The outlet is located at the top of the cyclone where a continuity condition is used for the gas phase. No particles are allowed to leave the circulating fluidized bed system. At the walls, no-slip conditions are used for the solid phases as well as the gas phase. A zero-flux boundary condition is applied to the energy fluxes.

## 4. Numerical results

### 4.1. Temporal evolutions

In order to study temporal variations of the gas/solid flow in the circulating fluidized bed, a 60-s real time simulation with a superficial gas velocity of  $0.7 \text{ m/s}$ , initial solids concentration of 1.0% and a particle size distribution with a standard deviation of  $18 \mu\text{m}$  is performed. The fluctuations are studied at the center axis, 1.0

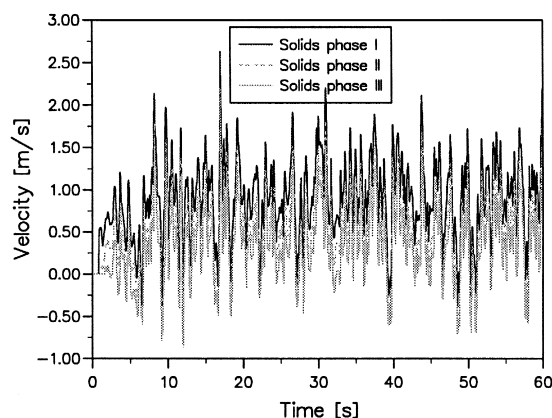


Fig. 4. Computed large solids scale velocity fluctuations,  $h = 1.0$  m,  $V_{\text{SUP}} = 0.7$  m/s.

m above the main gas inlet that is assumed to be located in the freeboard zone.

In Fig. 4, the computed velocity fluctuations of the three solid phases are presented, whereas the measured velocity fluctuations are reproduced in Fig. 5. As both figures show, the circulating fluidized bed never reach a normal steady state condition, but exhibits a strong fluctuating behavior. However, the simulation shows that the system needs almost 10 s to reach this condition. After the first 10 s the fluctuations have a constant mean value and frequency. Each of the solid phases has the same frequency and the relative velocity between the solid phases seems to be almost constant. As expected, the particle velocity increases with decreasing particle diameter. A somewhat wider range of velocity fluctuations is observed in the simulation compared with the measurements. The oscillating velocity includes negative and positive values, but at this position in the center of the riser, a much higher fraction of the particles are flowing upward than downward. The frequency of the fluctuations is in the same order of magnitude as the experimental, but they are a little bit higher in the measurements than in the simulation. This may be related to the observation that the measured velocity fluctuations include small scale as well as large scale

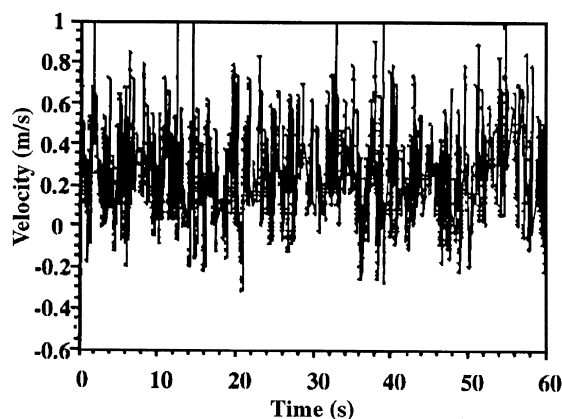


Fig. 5. Measured velocity solids fluctuations [9].

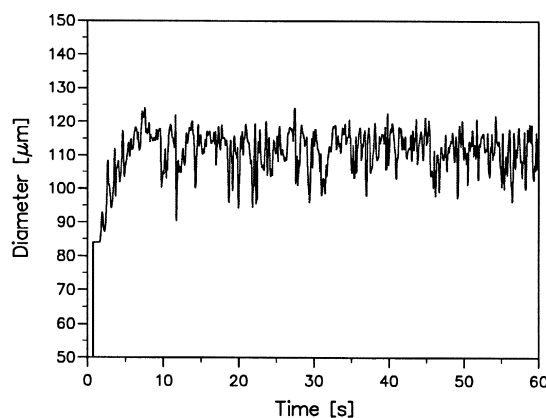


Fig. 6. Computed diameter fluctuations,  $h = 1.0$  m,  $V_{\text{SUP}} = 0.7$  m/s.

fluctuations, whereas the computed fluctuations are only produced by the large scale effects. A closer discussion of these large-scale fluctuations as well as the small scale will be treated later.

Computed and measured particle diameter fluctuations vs. time are plotted in Fig. 6 and Fig. 7, respectively. The mean diameters are in a fairly good agreement and the frequency of the fluctuations seems to be in the same order of magnitude. The measured oscillations are considerably larger than the computed. This is probably because the real particle size distribution is more wide-ranging than the numerical one. By increasing of number of solid phases, the oscillating diameter would have been more correctly predicted. It should be observed that particle diameters as large as 200  $\mu\text{m}$  and as small as 10  $\mu\text{m}$  are experimentally detected whereas the particle size distribution in Fig. 3 shows no particles above 160  $\mu\text{m}$  and below 50  $\mu\text{m}$ . The PDA technique is based upon the observation that the particles are smooth and spherical. Probably, some of the particles were not completely spherical and hence a small or large particle size was detected for these particular particles. If the spurious data were removed, comparison with the computations shown in Fig. 6 would be even better.

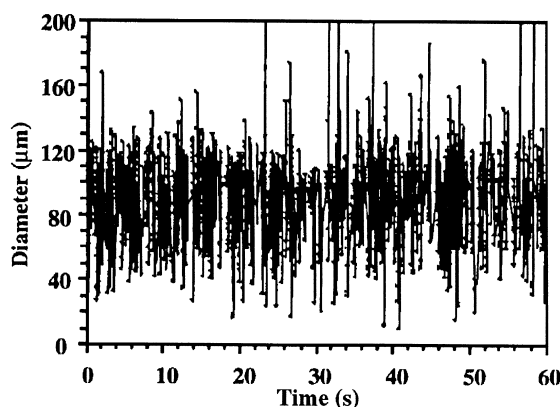


Fig. 7. Measured diameter fluctuations [9].

#### 4.2. Mean diameter profiles

A factor that significantly affects the magnitude of the segregation is the standard deviation of the particle size distribution. A narrow particle size distribution has obviously a more uniform mean diameter in a gas/solids flow system than a wider size distribution. Ref. [9] did a comparison of the mean diameters for two different particle size distributions with a constant mean diameter and showed a significant increase in axial segregation by size when the standard deviation increased.

Simulations are performed with the two different particle size distributions and compared against the experimental data in Fig. 8, which shows the number averaged mean diameter along the median axis of the riser. The superficial gas velocity and concentration of solids are held constant at 1.0 m/s and 3%, respectively. The simulation results are in a good agreement with the experimental data and have the same form. For the narrow size distribution ( $\sigma = 18 \mu\text{m}$ ), the particle size is almost constant along the median axis and only insignificant deviations from the experimental data are observed in the upper part of the riser. These deviations are probably caused by the difference in simulated and actual outlet geometry and 3D effects.

For the wide-ranging particle size distribution ( $\sigma = 40 \mu\text{m}$ ) the segregation by size is considerable. The multi-phase model calculates almost a correct level of segregation, although the predicted mean diameters are somewhat smaller than the measured. The computed mean diameters as well as the experimental data confirm that by using a large particle size distribution for the solids in the riser, an increase of the mass flow rate of fine particles will occur. Hence a lower mean particle diameter along the median axis is obtained.

#### 4.3. Velocity profiles

Ref. [9] measured axial velocity profiles in the free-board zone of the riser. The measurements were performed

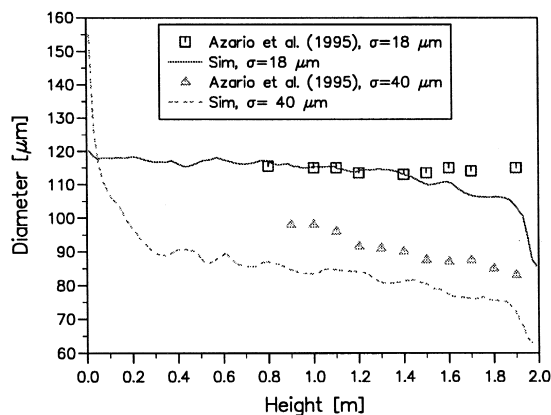


Fig. 8. Axial particle diameter profiles for different particle size distributions.

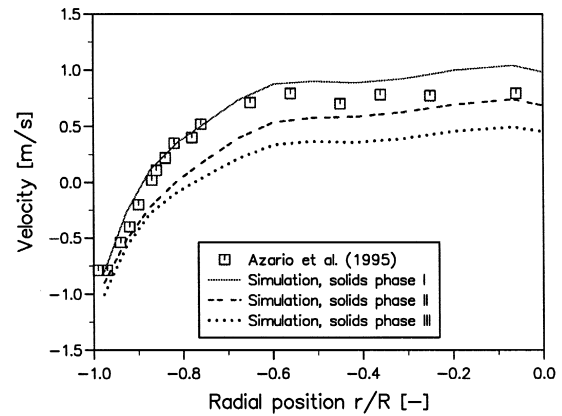


Fig. 9. Velocity profiles for different solids phases,  $h = 1.50 \text{ m}$ .

with a superficial gas velocity of 1.0 m/s, 3% initial volume fraction of solids and a standard deviation of the particle size distribution of  $18 \mu\text{m}$ .

Fig. 9 shows the particle velocity profiles for different solid phases at height 1.50 m above the primary gas inlet. Solid phases I, II and III have particle diameters of 84, 120 and 156, respectively. The computed velocity profiles are compared against a number averaged experimental velocity profile that does not separate between different particle sizes. As the figure shows, the agreement between the computed and experimental results are very well. A core-annulus flow, with an almost constant velocity in the core and a down-flow in the wall region, is obtained.

The different solid phases have a corresponding flow behavior. The simulation shows that the smallest particle have a larger velocity than the experimental, whereas the intermediate and largest particles have a lower velocity. The relative velocity between the largest and the middle particles is somewhat larger than between the intermediate and the smallest diameters. The relative velocity is approximately 0.2 m/s in the central part of the riser and decreases toward the wall.

An overall mean particle velocity from the individual solid phase velocities is obtained in order to compare this to the experimental one. The number averaged velocity is calculated from the following relation, where the subscripts indicate the solid phase number:

$$\bar{V}_s = \frac{\frac{\varepsilon_1}{d_1^3} V_1 + \frac{\varepsilon_2}{d_2^3} V_2 + \frac{\varepsilon_3}{d_3^3} V_3}{\frac{\varepsilon_1}{d_1^3} + \frac{\varepsilon_2}{d_2^3} + \frac{\varepsilon_3}{d_3^3}} \quad (26)$$

In Fig. 10, the predicted mean velocity profiles are compared against experimental data. The mean particle velocity profiles are obtained 1.20, 1.50 and 1.90 m above the primary gas inlet. The simulation is in good agreement with the measurements. At all three heights, the core-annulus flow is correctly predicted and only small deviations



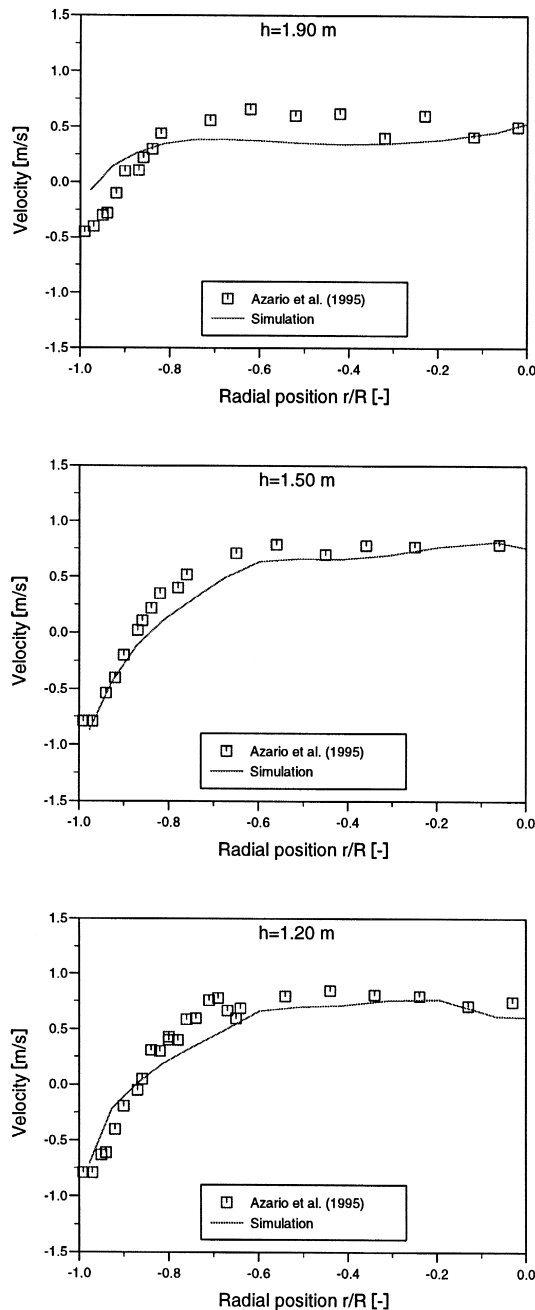


Fig. 10. Axial particle velocity profiles at different heights.

from the experimental data are observed. As in the experiments, the velocity profiles become flatter as the height above the inlet increases.

The radial mean velocity is plotted and compared against experimental data in Fig. 11. The radial velocity is obtained at height 1.20 m above the primary gas inlet and is plotted from the wall to the centerline. In this figure, the radial velocity is defined as positive toward the wall from the centerline. The numerical results are in good agreement with the experiments, both in form and magnitude. The radial velocity is very low in the center of the riser, but increases toward the shear layer. If the riser is symmetrical

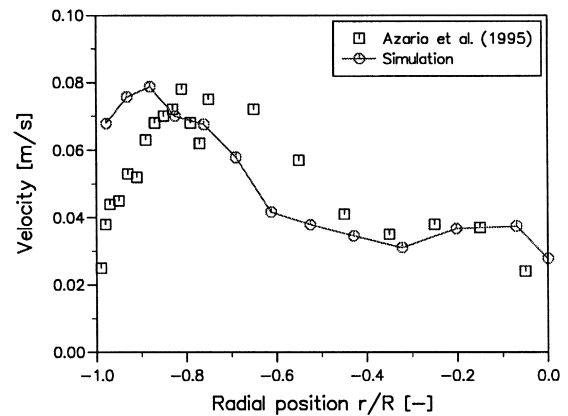


Fig. 11. Radial particle velocity,  $h = 1.20$  m.

about the median axis and a correct time averaging is performed, the radial velocity in the center should be zero. A small deviation from zero is found in the simulation.

Different particle size distributions will cause different mean velocities. In Fig. 12, the computed axial mean velocity along the median axis is compared against experimental data for the two particle size distributions with a standard deviation of 18 and 40  $\mu\text{m}$ , respectively. The simulations show the same trend as the experiments both in form and magnitude although some discrepancies are observed. The widest particle size distribution has the largest mean velocity at the centerline.

#### 4.4. Particle RMS velocity profiles

The Eulerian gas/particle flow model is based on the kinetic theory for granular flow. The equations come from interactions of the fluctuating and mean motion of the particles. These interactions generate stresses and give rise to effective viscosities for the solid phases that relate the random fluctuating motions to the mean motions of the solid phases. In the derivation of the kinetic theory and in the definition of the granular temperature, an isotropic

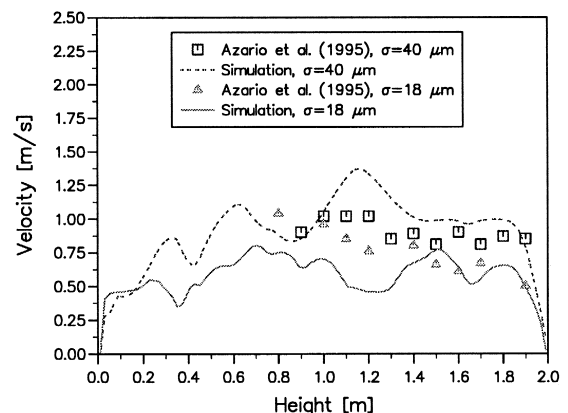
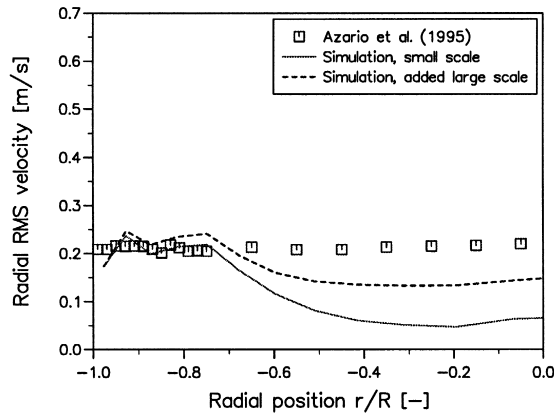


Fig. 12. Mean particle diameter along the median axis for different particle size distributions.

Fig. 13. Radial RMS velocities,  $h = 1.20$  m.

behavior of the particle fluctuations is assumed. Thus the axial and radial fluctuations should be the same. Ref. [9] showed experimentally that the magnitude of the axial and radial velocity fluctuations are quite different.

In the multiphase gas/solids flow model, a turbulent velocity is obtained for each solid phase and hence is not directly comparable to the experimental data. However, a number averaged granular temperature is estimated from the individual granular temperatures. The turbulent velocity obtained from this granular temperature is considered as the small-scale turbulence.

The large scale mean velocity fluctuations are shown in Fig. 4. The small- and large-scale fluctuations are assumed statistical independent and hence a total particle RMS velocity may be obtained:

$$V_{\text{RMS}} = \sqrt{3\bar{\theta}_s + \frac{\frac{\varepsilon_1}{d_1^3}\sigma_1^2 + \frac{\varepsilon_2}{d_2^3}\sigma_2^2 + \frac{\varepsilon_3}{d_3^3}\sigma_3^2}{\frac{\varepsilon_1}{d_1^3} + \frac{\varepsilon_2}{d_2^3} + \frac{\varepsilon_3}{d_3^3}}} \quad (27)$$

where the standard deviation  $\sigma_s$  of each solid phase is given by:

$$\sigma_s = \sqrt{\frac{1}{(N_i - 1)} \sum_{i=1}^{N_i} (v_i - \bar{v}_s)^2} \quad (28)$$

Experimental studies confirm a non-constitutive isotropic behavior of the fluctuations in a gas/solids flow system. In modelling of such systems, an assumption of isotropic granular temperature is not desirable if these fluctuations are the only oscillations of the system. However, it is reasonable to believe that the granular temperature only captures the small-scale fluctuations which will occur in a gas/solid system. The existence of large-scale fluctuations is clearly and evidently shown by Figs. 4–7 and is also easy to observe visually in a gas/solid flow system. That the simulation never reaches a normal steady state condition indicates also that there exist fluctuating effects as the granular temperature is not captured.

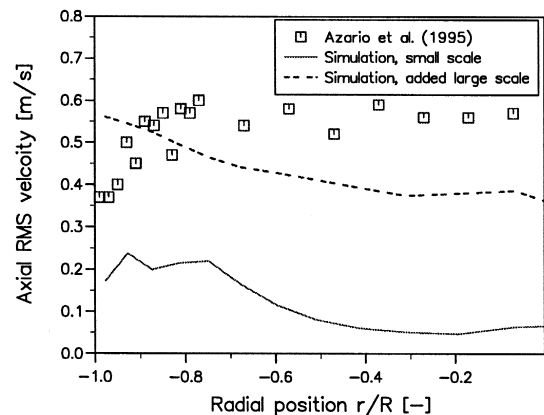
There is no doubt that large-scale as well as small-scale fluctuations are included in the measurements. Computed turbulent velocity from small- and large-scale fluctuations are compared against the experimental data in Figs. 13 and 14 for radial and axial direction, respectively.

Fig. 13 shows a significant difference in the computed radial RMS velocity whether the large scale fluctuations are added or not. The small-scale fluctuations have an almost constant value in the central part of the riser and increase significantly in the wall region. A comparison between the experimental data and the numerical small-scale turbulence shows that it is correctly predicted in the wall region, whereas quite significant discrepancies are obtained in the core region. In such a dilute gas/solid system considered in this simulation, the granular temperature is mainly produced by the shear forces, and hence largest in the annulus zone. When adding the large-scale turbulence, the curve changes both in form and magnitude. A more constant and correct turbulence behavior is obtained and the agreements with the measured RMS velocities are fairly well.

In Fig. 14 the experimental data show that the axial velocity fluctuations are approximately three times the radial RMS velocity. The computed small-scale turbulence is significantly too small according to the experimental data. By adding the large-scale turbulence, a correct order of magnitude is obtained although some deviations are still observed. Comparison of Figs. 13 and 14 shows that the large-scale fluctuations are significantly higher in the axial than in the radial direction.

#### 4.5. Mass flux profiles

Ref. [9] also measured and reported net mass flux profiles at three different heights. Particle flux profiles are computed and compared against these experimental data in Fig. 15. The computed fluxes are the sum of the individual solid phase fluxes. The flux profiles are obtained with a superficial gas velocity of 1.0 m/s, a standard deviation of

Fig. 14. Axial RMS velocities,  $h = 1.20$  m.

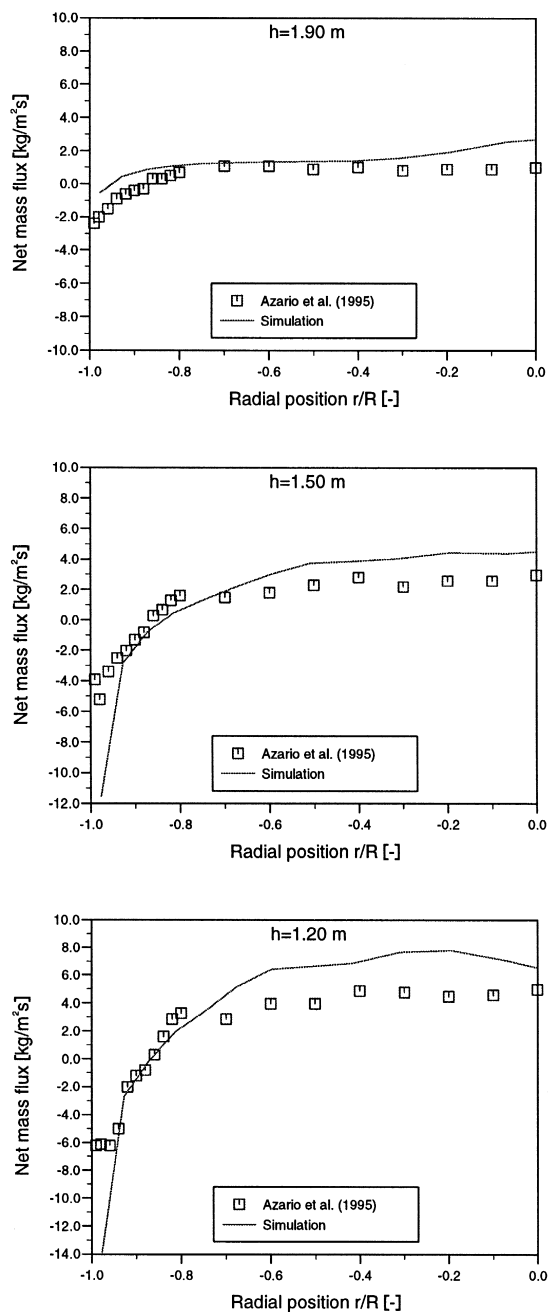


Fig. 15. Net solids flux profiles at different heights.

the particle size distribution of 18  $\mu\text{m}$ , 3% initial solids volume fraction, and 1.2, 1.5 and 1.9 m above the main gas inlet.

The simulation shows a fairly good agreement with the experimental data. Best agreement are obtained at a height 1.90 m above the primary gas inlet and this indicates that the total solids flux circulating in the loop is reasonably predicted.

At heights 1.20 and 1.50 m above the inlet, larger discrepancies are observed. The CFD model computes a too high flux upward in the core region, whereas a too high negative net flux is computed in the annulus region.

This result indicates that a too large axial mixing is computed, although the total net flux seems to be reasonable.

The particle velocity profiles presented in Fig. 10 showed a very good agreement with the experimental data. These profiles together with the net flux profiles indicate that the presence of solids at heights 1.2 and 1.5 m is somewhat too high. The volume fraction of solids is a little too high in the core as well as in the annulus region and probably the bed height is somewhat overpredicted.

## 5. Conclusions

Two-dimensional simulations of a pilot scale circulating fluidized bed are performed. The computational results are compared against experimental results reported in the literature. The simulations are performed with different superficial gas velocities, initial solids concentrations and standard deviations of the particle size distribution. Most emphasis is given to study the effects of different particle size distributions and to study the fluctuating behavior of the dilute gas/solids flow system. Altogether the simulation results are in very good agreement with experimental data.

The CFD model is shown to be able to capture the large scale fluctuations which will evidently be present in a circulating fluidized bed system. Axial and radial large-scale velocity fluctuations are calculated and added to the small-scale turbulence from the isotropic granular temperature. The computed small-scale turbulence is significantly too small according to the experimental data. By adding the large-scale fluctuations, a correct order of magnitude is obtained, although some discrepancies are still observed. The calculations confirm that the axial fluctuations are much larger than the radial fluctuations and hence the fluctuating behavior of the circulating fluidized bed is evidently not isotropic.

Simulations are performed with two different particle size distributions and compared against experimental data along the median axis of the riser. The computed mean diameters are in good agreement with the experimental data.

The axial velocity along the median axes are calculated for the two different particle size distributions as well. The simulations show the same tendency as the experiments, although some discrepancies are observed. A higher velocity is correctly obtained for the large particle size distribution.

Mean particle velocity profiles are obtained at three different heights with only insignificant deviations from the measurements. A typical core–annulus flow is calculated with a nearly constant velocity in the central part of the riser and a down flow of particles in the wall region. As in the experimental data, the velocity profiles became flatter when the height above the inlet increases.

A mean radial velocity is calculated as well. The agreement with experimental velocity is very well and the results show that the radial velocity is approximately zero at the centerline, then increases toward the shear layer and further decreases to the wall.

Net mass flux profiles are computed and presented. The calculated flux profiles show a fairly good agreement with the experimental data. Best agreement is obtained in the upper part of the riser and the total flux circulating in the loop seems to be reasonably predicted. At lower heights, larger deviations are obtained.

## 6. List of symbols

$C_d$	drag coefficient
$c_t$	constant in Sub Grid Scale model
$d$	particle diameter
$d_{sn}$	mean particle diameter = $0.5 (d_s + d_n)$
$e$	restitution coefficient
$e_{sn}$	mean restitution coefficient = $0.5 (e_s + e_n)$
$g_i$	$i$ -direction component of gravity
$g_0$	radial distribution function for a single solid phase
$g_{sn}$	binary radial distribution function
$l$	mean free path
$M$	number of phases
$m$	mass of a particle
$m_0$	binary mass = $m_s + m_n$
$N$	number of solid phases
$n$	number of particles
$P$	fluid pressure
$P_C$	collisional pressure
$P_s$	solid phase pressure
$Re_s$	particle Reynolds number
$U_i, U_j$	$i$ - and $j$ -components of velocity
$\vec{u}$	velocity vector
$V$	particle velocity

### Greek symbols

$\varepsilon$	volume fraction
$\varepsilon_{s,max}$	maximum total volume fraction of solids
$\beta_i$	area porosity in $i$ -direction
$\beta_v$	volume porosity
$\gamma$	collisional energy dissipation
$\delta_{ij}$	Kronecker delta
$\theta$	granular temperature = $1/3 \langle C_s^2 \rangle$
$\kappa$	transport coefficient of granular temperature
$\mu$	shear viscosity
$\xi$	bulk viscosity
$\Pi_{ij}$	stress tensor, solid phase
$\rho$	density
$\sigma$	standard deviation
$\tau_{ij,g}$	stress tensor, gas phase
$\Phi$	drag coefficient

## Subscripts

av	average
col	collisional
cor	correction
dil	dilute
eff	effective
g	gas phase
kin	kinetic
lam	laminar
m	gas phase or solid phase m
n	solid phase n
RMS	Root Mean Square
s	solid phase s
SUP	superficial
turb	turbulent

## Acknowledgements

The authors would like to express their thanks to Norsk Hydro, Statoil and The Research Council of Norway (NFR) for their financial support of this work.

## References

- [1] D. Gidaspow, *Multiphase Flow and Fluidization*, Academic Press, Boston, 1994.
- [2] E. Helland, T. Van den Moortel, R. Occelli, L. Tadrist, B.H. Hjertager, T. Solberg, V. Mathiesen, in: J. Werther (Ed.), *Circulating Fluidized Bed Technology VI*, DECHEMA, Frankfurt, Germany, 1999, p. 261.
- [3] H. Enwald, E. Peirano, A.-E. Almstedt, *Int. J. Multiphase Flow* 22 (1996) 21.
- [4] J.T. Jenkins, F. Mancini, *J. Appl. Mech.* 54 (1987) 27.
- [5] V. Mathiesen, T. Solberg, E. Manger, B.H. Hjertager, in: J. Kwauk, L. Li (Eds.), *Circulating Fluidized Bed Technology V*, Science Press, Beijing, China, 1997, p. 426.
- [6] D. Gidaspow, L. Huilin, E. Manger, *XIXth Int. Cong. of Theoretical and Appl. Mech.*, Japan, 1996.
- [7] E. Manger, PhD-thesis, Telemark College, Norway, 1996.
- [8] V. Mathiesen, T. Solberg, B.H. Hjertager, *Int. J. Multiphase Flow* 26 (2000) 387.
- [9] E. Azario, L. Tadrist, R. Santinini, J. Pantaloni, *Proc. of the 2nd Int. Conference on Multiphase Flow*, Japan Vol. 41995.
- [10] J.W. Deardorff, *J. Comp. Phys.* 7 (1971) 120.
- [11] Y. Yakhot, S.A. Orszag, *J. Scientific Comput.* 1 (1986) 3.
- [12] R.A. Bagnold, *Proc. R. Soc. A* 255 (1954) 49.
- [13] S. Ergun, *Chem. Eng. Prog.* 48 (1952) 89.
- [14] C.Y. Wen, Y.H. Yu, *Chem. Eng. Prog. Symp. Ser.* 62 (1966) 100.
- [15] D. Gidaspow, B. Ettehadieh, *I&EC Fundam.* 22 (1983) 193.
- [16] P.N. Rowe, *Trans. Inst. Chem.* 39 (1961) 175.
- [17] D.B. Spalding, in: R.W. Lewis, K. Morgan, J.A. Johnson, W.R. Smith (Eds.), *Computational Techniques in Heat Transfer*, Pineridge Press, 1985, pp. 1–44.
- [18] D.B. Spalding, *Numerical Properties and Methodologies in Heat Transfer*, Hemisphere Publishing, 1983, pp. 421–476.
- [19] A. Samuelsen, B.H. Hjertager, *Int. J. Multiphase Flow* 22 (1996) 575.
- [20] A. Samuelsen, B.H. Hjertager, *AIChE J.* 42 (1996) 1536.